Experimental Observation of Aharonov-Bohm Cages in Photonic Lattices

Sebabrata Mukherjee,[1,*] Marco Di Liberto,[2] Patrik Öhberg,[1] Robert R. Thomson,[1] and Nathan Goldman[2]

[1]*Scottish Universities Physics Alliance (SUPA), Institute of Photonics and Quantum Sciences,*
School of Engineering and Physical Sciences, Heriot-Watt University, Edinburgh EH14 4AS, United Kingdom
[2]*Center for Nonlinear Phenomena and Complex Systems, Université Libre de Bruxelles,*
CP 231, Campus Plaine, B-1050 Brussels, Belgium

We report on the experimental realization of a uniform synthetic magnetic flux and the observation of Aharonov-Bohm cages in photonic lattices. Considering a rhombic array of optical waveguides, we engineer modulation-assisted tunneling processes that effectively produce nonzero magnetic flux per plaquette. This synthetic magnetic field for light can be tuned at will by varying the phase of the modulation. In the regime where half a flux quantum is realized in each plaquette, all the energy bands dramatically collapse into nondispersive (flat) bands and all eigenstates are completely localized. We demonstrate this Aharonov-Bohm caging by studying the propagation of light in the bulk of the photonic lattice. Besides, we explore the dynamics on the edge of the lattice and discuss how the corresponding edge states can be continuously connected to the topological edge states of the Creutz ladder. Our photonic lattice constitutes an appealing platform where the interplay between engineered gauge fields, frustration, localization, and topological properties can be finely studied.

Introduction.—The investigation of electron transport in crystals subjected to external magnetic fields has led to the discovery of many intriguing phenomena including the integer and fractional quantum Hall effects [1,2]. In recent years, inspired by the idea of quantum simulation [3], there has been a growing interest in realizing and exploiting synthetic magnetic fields for electrically neutral particles in artificial crystals, such as cold atoms in optical lattices [4–6]. Synthetic magnetic fields have also been realized for photons, thus paving the way to the emergent field of topological photonics [7–9]. For example, a uniform magnetic field has been realized using off-resonantly coupled ring resonators [10], and a strain-induced pseudomagnetic field has been demonstrated in coupled-waveguide arrays [11]. Additionally, Landau levels physics has been explored in a multimode ring resonator through the realization of a fictitious Lorentz (or Coriolis) force acting on photons [12].

The quantum properties of a charged particle moving in a magnetic field find their origin in the Aharonov-Bohm (AB) phase [13,14], namely, the phase acquired by the wave function of the particle as it performs a loop around a spatial region containing a nonzero magnetic flux. Direct evidence of this AB phase has been experimentally demonstrated in electronic systems [15], and more recently, in photonics [16,17] and ultracold atoms [18]. Interestingly, for certain geometries and specific values of transverse magnetic fields, noninteracting particles can exhibit *complete localization* [19,20] due to destructive interferences of the wave function. This AB caging phenomenon, which

was found to occur in the $\mathcal{T}_3$ (or dice) and the rhombic lattice, is distinct from Anderson localization [21], which is instead caused by disorder. An experimental signature of this phenomenon was reported in solid state, by detecting a depression of the critical current and that of the superconducting-transition temperature in a network of superconducting wires [22], and also by magnetoresistance measurements in normal metal networks [23].

Here, we demonstrate the first experimental realization of a uniform synthetic magnetic flux in ultrafast-laser-fabricated waveguide arrays, and use this setting to observe AB cages for light. The idea of creating and controlling a synthetic magnetic flux for photons propagating in a lattice was first proposed in Ref. [24], where a periodic modulation of the intersite tunneling amplitudes was shown to realize complex effective tunneling matrix elements; see also Refs. [25,26]. In this Letter, we follow another approach [25], and apply a linear detuning of the propagation constants along the lattice, in order to suppress the effective intersite tunneling; this tunneling is then restored and controlled by resonantly modulating the propagation constants with a desired phase of modulation. Complex-valued tunneling matrix elements and a nonzero synthetic magnetic flux are successfully generated through this resonant modulation-assisted tunneling process. We build on this scheme to realize AB cages for photons evolving on a rhombic geometry [Fig. 1(a)]. In the caging limit, which is reached when each plaquette is associated with a flux of π, all the energy bands of the lattice become dispersionless (flat). By launching input states that overlap with these
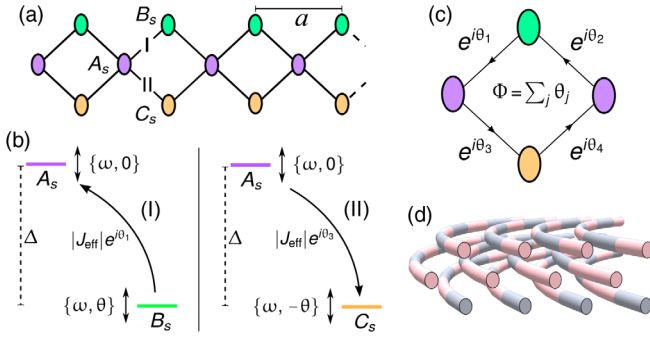
FIG. 1.   (a) Schematic diagram of a rhombic (or diamond) lattice with three sites (A, B, and C) per unit cell. (b) Complex-valued tunneling amplitudes are generated by applying a linear gradient of on-site energy Δ along the lattice and then periodically modulating the on-site energies with frequency $\omega = \Delta$ and phase θ, see Fig. 2(a). (c) In this driving protocol, a nonzero synthetic magnetic flux (Φ) per plaquette is realized and it can be tuned by varying the phase of modulation θ. (d) Simplified sketch illustrating the 3D waveguide paths of a driven photonic rhombic lattice with $\Phi = \pi$ flux per plaquette. The linear gradient of on-site energy is realized by circularly curving the lattice. Here, the color contrast indicates a square wave modulation of the on-site energy.

flatbands, we observe breathing motions of the optical intensity, which clearly signal photonic AB caging. We then demonstrate that the overall bandwidth of the spectrum can be well controlled by varying the driving parameters. We also present the dynamics of the states localized on the edge, which can be continuously connected to the topological midgap edge states of the Creutz ladder [27,28].

Driving protocol.—Consider a quasi-1D rhombic lattice [20,25,29–31] with three sites (A, B, and C) per unit cell, Fig. 1(a). In the tight-binding approximation, the single-particle Hamiltonian with only nearest-neighbor tunneling processes reads

$$\hat{H}_0 = -J\sum_s (\hat{a}_s^\dagger \hat{b}_s + \hat{a}_s^\dagger \hat{c}_s + \hat{a}_s^\dagger \hat{b}_{s-1} + \hat{a}_s^\dagger \hat{c}_{s-1} + \text{H.c.}), \quad (1)$$

where J is the tunneling amplitude between neighboring sites, $\hat{a}_s^\dagger$, $\hat{b}_s^\dagger$ and $\hat{c}_s^\dagger$ ($\hat{a}_s$, $\hat{b}_s$, and $\hat{c}_s$) are the creation (annihilation) operators for a particle at the A, B, and C sites of the sth unit cell, respectively. This lattice supports three energy bands, two of them are dispersive and the third one is perfectly flat at zero energy [31]. To realize complex-valued tunneling amplitudes leading to a nonzero magnetic flux per plaquette, the Hamiltonian of the system is engineered in the following way. First, the on-site energies are linearly detuned along the lattice

$$\hat{H}_d = -\Delta \sum_s [2s\hat{a}_s^\dagger \hat{a}_s + (2s+1)\hat{b}_s^\dagger \hat{b}_s + (2s+1)\hat{c}_s^\dagger \hat{c}_s], \quad (2)$$

where Δ is the on-site energy shift between nearest-neighbor sites, which is considered to be large, $\Delta \gg J$,

to inhibit effective tunneling (an effect known as Wannier-Stark localization [32]). The on-site energy offsets are then independently and periodically modulated in time

$$\hat{H}_{\text{AC}} = \frac{K}{2}\sum_s [f(\omega t)\hat{a}_s^\dagger \hat{a}_s + f(\omega t + \theta)\hat{b}_s^\dagger \hat{b}_s + f(\omega t - \theta)\hat{c}_s^\dagger \hat{c}_s], \quad (3)$$

where K and $\omega(\equiv 2\pi/T)$ are the peak-to-peak amplitude and frequency of a square wave modulation (f), respectively, $+\theta$ ($-\theta$) is the relative phase of modulation between the A and B (C) sites. Considering the total time-dependent Hamiltonian, $\hat{H}(t) = \hat{H}_0 + \hat{H}_d + \hat{H}_{\text{AC}}$, a resonant AC modulation (i.e., $\Delta = \omega\nu$ where $\nu \in \mathbb{Z}$) can restore effective tunneling processes [25], as depicted in Fig. 1(b). The quasienergy spectrum for this periodically driven system is obtained by diagonalizing the Floquet or effective Hamiltonian, $\hat{H}_{\text{eff}} \equiv (i/T) \log \hat{U}(T)$, where the time-evolution operator over one period is defined as $\hat{U}(T) = \mathcal{T} \exp[-i \int_0^T \hat{H}(t')dt']$, $\mathcal{T}$ indicates the time ordering, and T is the period of driving [33,34].

In the high-frequency limit $\omega \gg J$ and for a resonant modulation, one can employ standard methods [33,34] to calculate a systematic expansion in $1/\omega$ of the operator $\hat{H}_{\text{eff}}$. The lowest order of this expansion is of the form

$$\hat{H}_{\text{eff}}^{(0)} = |J_{\text{eff}}|\sum_s \Big(e^{i\theta_1}\hat{a}_s^\dagger \hat{b}_s + e^{-i\theta_2}\hat{a}_s^\dagger \hat{b}_{s-1} + e^{-i\theta_3}\hat{a}_s^\dagger \hat{c}_s$$
$$+ e^{i\theta_4}\hat{a}_s^\dagger \hat{c}_{s-1} + \text{H.c.}\Big), \quad (4)$$

where the restored tunneling amplitudes are now complex valued and a nonvanishing constant flux $\Phi = \sum_j \theta_j$ is realized in each plaquette [Fig. 1(c)].

Figure 2(a) shows how the synthetic flux Φ and the modulus of the effective tunneling amplitude $|J_{\text{eff}}|$ vary as a function of the phase of modulation θ. The AB caging condition that yields a full localization of the eigenstates is met when $\Phi = \pi$, i.e., when the phase of modulation is $\theta = \pi/2$ or $\theta = 3\pi/2$. The exact Floquet quasienergy spectrum obtained from the diagonalization of $\hat{H}_{\text{eff}}$ is shown in Fig. 2(b) as a function of K/ω for the caging limit, $\theta = \pi/2$. Figure 2(c) presents a comparison of the exact quasienergy spectrum for the experimentally realized drive frequency (see below), $\omega/J = 12.64$, and the one obtained from $\hat{H}_{\text{eff}}^{(0)}$ in Eq. (4), thus indicating that the high-frequency approximation is valid for our experiments.

In the AB caging limit ($\Phi = \pi$), the spectrum displays three nondispersive bulk bands, Figs. 2(b)–2(c). One band is at energy $\varepsilon_0^{\text{bulk}} = 0$ and the localized eigenstates read $|\psi_{s,0}^{\text{bulk}}\rangle = (\hat{b}_{s-1}^\dagger + \hat{c}_{s-1}^\dagger + \hat{b}_s^\dagger - \hat{c}_s^\dagger)|0\rangle$; the eigenstates are given in a gauge where the tunneling phases entering the Hamiltonian in Eq. (4) are $\theta_1 = \pi$ and $\theta_{2-4} = 0$. The other
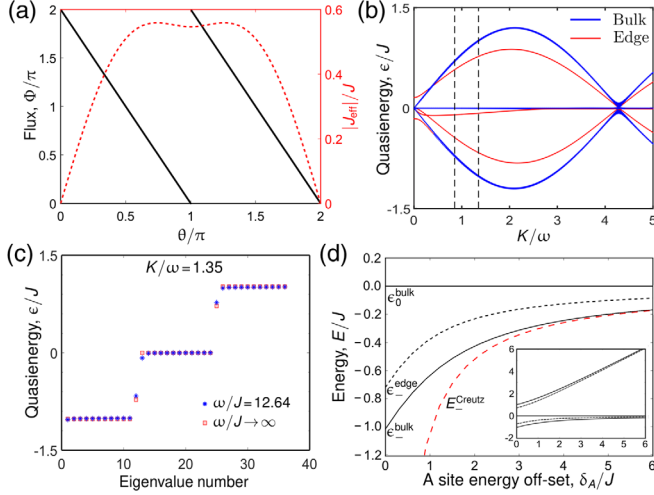
FIG. 2. (a) Variation of flux and the modulus of effective tunneling amplitude as a function of the phase of modulation (θ) for $K/\omega = 1.35$. (b) Quasienergy spectrum for a finite rhombic chain with $\theta = \pi/2$. Blue and red colors are associated with the bulk and edge modes, respectively. The dashed vertical lines indicate the values of K/ω (1.35 and 0.85) that were realized in the experiment. (c) A comparison of the Floquet quasienergy spectrum for $\omega/J = 12.64$ and $\omega/J \to \infty$. Here, $K/\omega = 1.35$. (d) Zoom of the energy spectrum of $\hat{H}_{\mathrm{eff}}^{(0)}$ with an additional detuning δ_A of the on-site energy at A sites (full spectrum shown in the inset). The red dashed line is the energy ($E_-^{\mathrm{Creutz}} = -4J_{\mathrm{eff}}^2/\delta_A$) of the lowest flatband of the Creutz ladder into which we map $\hat{H}_{\mathrm{eff}} + \hat{H}_{\delta_A}$ for $\delta_A \gg J_{\mathrm{eff}}$. The upper flatband of the Creutz ladder is at energy $E_+^{\mathrm{Creutz}} = 0$. The black dotted line corresponds to the edge state, which becomes a topological midgap state (protected by an emergent chiral symmetry) in the Creutz-ladder limit $\delta_A \gg J_{\mathrm{eff}}$. Parameters are chosen as in (c).

two bands appear at energies $\epsilon_\pm^{\mathrm{bulk}} = \pm 2|J_{\mathrm{eff}}|$ and the eigenstates are $|\psi_{s,\pm}^{\mathrm{bulk}}\rangle = (\hat{b}_{s-1}^\dagger + \hat{c}_{s-1}^\dagger \mp 2\hat{a}_s^\dagger - \hat{b}_s^\dagger + \hat{c}_s^\dagger)|0\rangle$. In Fig. 2(b), we also see the appearance of states that are localized at the edges (highlighted by red lines). Indeed, when open boundary conditions are considered, such that the rhombic chain has an edge with an A site termination, the effective model (4) predicts a pair of states with energies $\epsilon_\pm^{\mathrm{edge}} = \pm\sqrt{2}|J_{\mathrm{eff}}|$; for the left edge of the chain, the eigenstates read $|\psi_{1,\pm}^{\mathrm{edge}}\rangle = (\mp\sqrt{2}a_1^\dagger - b_1^\dagger + c_1^\dagger)|0\rangle$. Similarly, a pair of edge states would appear on the right edge [35].

Interestingly, the edge states of the rhombic chain with π flux per plaquette can be continuously connected to the topological midgap edge state of the Creutz ladder [27,28]. This can be seen by adding an on-site offset $\hat{H}_{\delta_A} = \delta_A \sum_s \hat{a}_s^\dagger \hat{a}_s$ and by considering the limit $\delta_A \gg J_{\mathrm{eff}}$; see Fig. 2(d) and [36] for more details on this mapping.

Experiments.—Our experimental platform consists of photonic lattices—periodic arrays of evanescently coupled optical waveguides—fabricated using ultrafast laser inscription [36,37]. Finite rhombic lattices with twelve unit cells were fabricated with a waveguide-to-waveguide

separation $a/\sqrt{2} = 17 \ \mu m$. In the scalar-paraxial approximation [38–40], the evolution of the optical field along the propagation distance (z) of our photonic lattices is formally equivalent to the time evolution of a single particle wave function obeying the discrete Schrödinger equation associated with the Hamiltonian $\hat{H}_0$ in Eq. (1). By characterizing a set of directional couplers (two identical evanescently coupled waveguides) at 780 nm wavelength, we obtained the analogous tunneling strength, $J = 0.035 \pm 0.002 \ \mathrm{mm}^{-1}$ entering Eq. (1). The next-nearest-neighbor and higher-order tunneling processes were insignificant for the maximum propagation distance considered in this work. Within the mapping described above, the propagation constants of the optical modes play the role of on-site energies. Hence, the Hamiltonian $\hat{H}_d$ in Eq. (2) can be simulated by applying a linear gradient to the propagation constants; here this is obtained by circularly curving the axes of the waveguides in the photonic lattice [32,41,42]. Specifically, a radius of curvature R leads to an energy shift $\Delta = n_0 a/(2R\lambdabar)$ in Eq. (2), where n_0 is the average refractive index of the substrate and $\lambda = 2\pi\lambdabar$ is the free-space wavelength of light. The driving term $\hat{H}_{\mathrm{AC}}$ in Eq. (3) is then mimicked by applying a spatial square-wave modulation of the propagation constants, which is realized by varying the translation speed of fabrication; see Fig. 1(d) and [36]. In our experiment, this modulation has a period $z_0 = 2\pi/\omega = 14 \ \mathrm{mm}$, and it does not significantly affect the intersite tunneling strength [43,44]. The peak-to-peak amplitude of the square wave modulation (K) was measured by characterizing a set of straight directional couplers fabricated with modulated translation speeds $[v_1 = (v_0/2)f(\omega z)$ and $v_2 = (v_0/2)f(\omega z + \pi)]$; see [36]. The final modulated lattices with circularly curved paths were fabricated inside a 70-mm-long borosilicate substrate using two sets of extrema of translation speeds, $\{v_{\max}, v_{\min}\} = \{9, 6\} \ \mathrm{mm/s}$ and $\{9, 7\} \ \mathrm{mm/s}$, which leads to the parameters values $K/\omega = 1.35$ and 0.85, respectively [see Eq. (3)]. Besides, in all the experiments described below, the resonance condition was set to $\Delta = \omega = 12.64J$.

The evolution of the optical intensity governed by the static Hamiltonian in Eq. (1), in the absence of driving ($K = 0$ and $\Delta = 0$), is presented in [36]; see also the inset in Fig. 3. As shown in Fig. 2(a), the synthetic magnetic flux can be activated in a modulated lattice, where it can be tuned by varying the phase of modulation. In [36], we have presented the evolution of an input state, localized on a bulk A site, with phases of modulation $\theta = \pi/5$ and π. Here in the main text, we focus on a specific value of flux, $\Phi = \pi$, for which optical waves tunneling along a closed loop on the lattice acquire a nonvanishing AB-type phase of π, thus realizing the photonic AB-caging regime. In our experiments, the maximum achievable strength of on-site modulation, which does not affect the tunneling strength, was found to be $K = 1.35\omega$. In this situation,
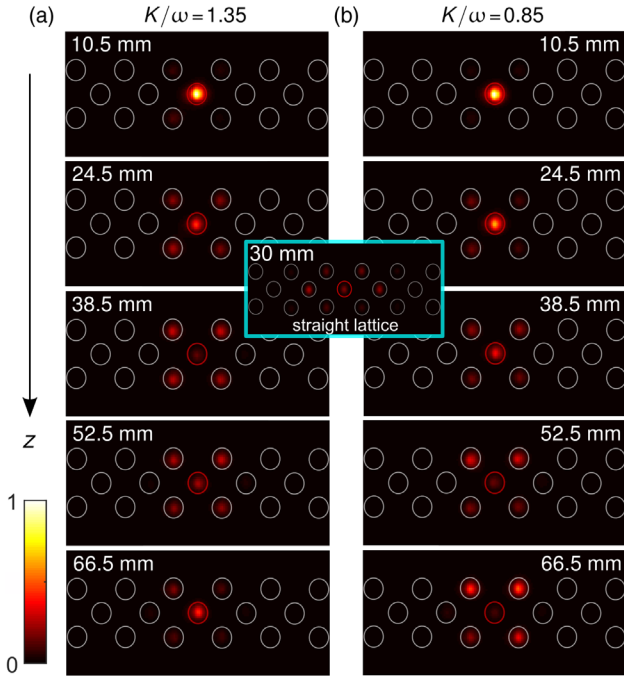
FIG. 3. Observation of Aharonov-Bohm photonic caging in the presence of $\Phi = \pi$ magnetic flux per plaquette. Experimentally measured output intensity distributions at five different propagation distances (shown on each image) for $K/\omega = 1.35$ (a) and $K/\omega = 0.85$ (b). The optical intensity exhibits a breathing motion whose frequency is determined by K/ω. For all measurements, light was injected at the red circled A site—this input state overlaps efficiently with the upper and lower flatbands and the frequency of the observed breathing motion is related to the energy gap between these two bands. Each image is normalized so that the total intensity is 1. The field of view is approximately $121\ \mu m \times 61\ \mu m$. The inset shows the spreading (delocalization) of the optical intensity in a straight lattice (i.e., $\Phi = 0$); see [36].

$\Phi = \pi$ magnetic flux per plaquette is realized for a phase $\theta = \pi/2$ and the effective tunneling strength becomes $|J_{\rm eff}| = 0.509J$; see Fig. 2(a).

By launching light at 780 nm wavelength into a bulk A site, we excite a superposition of the upper and lower flatband states and observe a breathing motion of the optical intensity, as shown in Fig. 3(a). In this case, the expected period of oscillation, determined by the energy gap between the upper and lower flatbands, is $\pi/(2|J_{\rm eff}|) \approx 88$ mm. The optical intensity is trapped at the initially excited A site and its four nearest neighbor sites due to the AB caging phenomenon. To demonstrate the tunability of the overall bandwidth of the spectrum, we perform another set of experiments with $K/\omega = 0.85$ and $\theta = \pi/2$, implying $J_{\rm eff}/J = 0.357$, see Fig. 3(b). In this case, the frequency of the breathing motion is relatively lower, which reflects the smaller bandwidth of the spectrum; specifically, the expected period of oscillation is $\pi/(2|J_{\rm eff}|) \approx 124$ mm. Figure 4(a) shows the comparison between the measured and expected variation of the optical
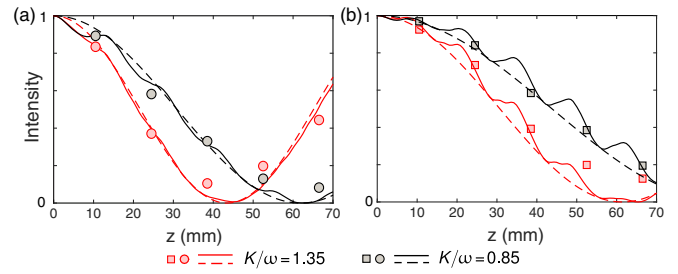

FIG. 4. (a) Graphical representation of Fig. 3. The dashed and solid lines indicate the z evolution of optical intensities (at the initially excited bulk A site), which were numerically calculated solving the Schrödinger equation for $\omega/J = 12.64$ associated with the Hamiltonians $\hat{H}_{\rm eff}$ and $\hat{H}(t \leftrightarrow z)$, respectively. Small oscillations can be observed as a consequence of micromotion. The filled circles indicate the measured light intensities at the A site. See also Fig. A3 in [36]. (b) Edge dynamics—when light is launched at the A site on the edge, the input state overlaps with edge modes located in both band gaps. In this case, a breathing motion with relatively lower frequency (compared to the bulk excitation) was observed, as expected. Indeed, the frequency of this breathing motion is associated with the energy difference between the edge modes [see Fig. 2(c)].

intensities at the initially excited bulk A site—here, the dashed and solid lines indicate the z evolution of the optical intensities which were numerically calculated for $\omega/J = 12.64$ by solving the Schrödinger equation associated with the Hamiltonians $\hat{H}_{\rm eff}$ and $\hat{H}(t \leftrightarrow z)$, respectively. In the experiment, the oscillation frequency was estimated from the half of the total period of oscillation, i.e., the propagation distance at which the intensity at the initially excited A site becomes minimal (≈ 0). To further confirm the existence of three flatbands (AB caging), we launched light into a single bulk C site, which has nonzero overlap with all three bands. In that case, the observed oscillations clearly revealed two frequencies, in agreement with the two relevant energy separations of the spectrum in Fig. 2(c); see [36].

In the next step, we launch light at the A site on the edge—this input state efficiently overlaps with the edge modes located in both band gaps. In the experiment, the optical intensity was observed to oscillate among the A site (where light was initially launched) and its two neighboring B and C sites. As the energy gap between these edge modes is smaller compared to that between the upper and lower flatbands [Fig. 2(c)], we observe a breathing motion of optical intensity with relatively lower frequency (compared to the bulk A site excitation), see Fig. 4(b).

Conclusion.—We have experimentally demonstrated the realization of a uniform synthetic magnetic flux in ultrafast-laser-fabricated rhombic lattices. This driving protocol can be extended to realize a uniform flux in 2D lattices, such as the square lattice, indicating an exciting route towards the experimental realization of the Hofstadter spectrum [45] and associated topological phenomena [46] in photonic

lattices. In addition, the experimental platform offered by photonic lattices allows one to address and control specific lattice sites independently, which enables the realization and manipulation of magnetic flux on each individual plaquette; this makes the creation of spatially periodic or even random flux configurations [47,48] accessible in experiments.

Realizing synthetic magnetic flux for light has allowed us to observe AB caging in photonic lattices, an effect that originates from the isolated flatbands of the underlying spectrum. This is to be contrasted with other models that were previously implemented in the absence of magnetic flux, e.g., the static rhombic lattice [31] or the Lieb lattice [49,50], where flatbands always appear together with dispersive ones. We stress that these previous setups required specific state preparations to observe localization. Interestingly, in the case of AB caging, the role of interactions is enormously enhanced [51–53], even at the mean-field level, and it can lead to nontrivial states of matter where, for instance, time-reversal symmetry is spontaneously broken [54]. This possibility therefore paves the way to investigate the impact of optical nonlinearities in fully gapped flatband systems [9,55].

Raw experimental data are available in Ref. [56].

Note added.—After completion of this work, we were made aware of similar results reported in Ref. [57].

*mukherjeesebabrata@gmail.com

[1] K. v. Klitzing, G. Dorda, and M. Pepper, Phys. Rev. Lett. **45**, 494 (1980).

[2] D. C. Tsui, H. L. Stormer, and A. C. Gossard, Phys. Rev. Lett. **48**, 1559 (1982).

[3] R. P. Feynman, Int. J. Theor. Phys. **21**, 467 (1982).

[4] Y.-J. Lin, R. L. Compton, K. Jimenez-Garcia, J. V. Porto, and I. B. Spielman, Nature (London) **462**, 628 (2009).

[5] M. Aidelsburger, M. Atala, M. Lohse, J. T. Barreiro, B. Paredes, and I. Bloch, Phys. Rev. Lett. **111**, 185301 (2013).

[6] H. Miyake, G. A. Siviloglou, C. J. Kennedy, W. C. Burton, and W. Ketterle, Phys. Rev. Lett. **111**, 185302 (2013).

[7] L. Lu, J. D. Joannopoulos, and M. Soljačić, Nat. Photonics **8**, 821 (2014).

[8] A. B. Khanikaev and G. Shvets, Nat. Photonics **11**, 763 (2017).

[9] T. Ozawa, H. M. Price, A. Amo, N. Goldman, M. Hafezi, L. Lu, M. Rechtsman, D. Schuster, J. Simon, O. Zilberberg, and I. Carusotto, arXiv:1802.04173.

[10] M. Hafezi, S. Mittal, J. Fan, A. Migdall, and J. Taylor, Nat. Photonics **7**, 1001 (2013).

[11] M. C. Rechtsman, J. M. Zeuner, A. Tünnermann, S. Nolte, M. Segev, and A. Szameit, Nat. Photonics **7**, 153 (2013).

[12] N. Schine, A. Ryou, A. Gromov, A. Sommer, and J. Simon, Nature (London) **534**, 671 (2016).

[13] Y. Aharonov and D. Bohm, Phys. Rev. **115**, 485 (1959).

[14] T. T. Wu and C. N. Yang, Phys. Rev. D **12**, 3845 (1975).

[15] R. Chambers, Phys. Rev. Lett. **5**, 3 (1960).

[16] N. Satapathy, D. Pandey, P. Mehta, S. Sinha, J. Samuel, and H. Ramachandran, Europhys. Lett. **97**, 50011 (2012).

[17] E. Li, B. J. Eggleton, K. Fang, and S. Fan, Nat. Commun. **5**, 3225 (2014).

[18] L. Duca, T. Li, M. Reitter, I. Bloch, M. Schleier-Smith, and U. Schneider, Science **347**, 288 (2015).

[19] J. Vidal, R. Mosseri, and B. Douçot, Phys. Rev. Lett. **81**, 5888 (1998).

[20] J. Vidal, B. Douçot, R. Mosseri, and P. Butaud, Phys. Rev. Lett. **85**, 3906 (2000).

[21] P. W. Anderson, Phys. Rev. **109**, 1492 (1958).

[22] C. C. Abilio, P. Butaud, T. Fournier, B. Pannetier, J. Vidal, S. Tedesco, and B. Dalzotto, Phys. Rev. Lett. **83**, 5102 (1999).

[23] C. Naud, G. Faini, and D. Mailly, Phys. Rev. Lett. **86**, 5104 (2001).

[24] K. Fang, Z. Yu, and S. Fan, Nat. Photonics **6**, 782 (2012).

[25] S. Longhi, Opt. Lett. **39**, 5892 (2014).

[26] A. Spracklen, Ph.D. thesis, Heriot-Watt University, 2018.

[27] M. Creutz, Phys. Rev. Lett. **83**, 2636 (1999).

[28] J. Jünemann, A. Piga, S.-J. Ran, M. Lewenstein, M. Rizzi, and A. Bermudez, Phys. Rev. X **7**, 031057 (2017).

[29] C. E. Creffield and G. Platero, Phys. Rev. Lett. **105**, 086804 (2010).

[30] R. Khomeriki and S. Flach, Phys. Rev. Lett. **116**, 245301 (2016).

[31] S. Mukherjee and R. R. Thomson, Opt. Lett. **40**, 5443 (2015).

[32] S. Mukherjee, A. Spracklen, D. Choudhury, N. Goldman, P. Öhberg, E. Andersson, and R. R. Thomson, New J. Phys. **17**, 115002 (2015).

[33] N. Goldman, J. Dalibard, M. Aidelsburger, and N. R. Cooper, Phys. Rev. A **91**, 033632 (2015).

[34] A. Eckardt and E. Anisimovas, New J. Phys. **17**, 093039 (2015).

[35] The small energy asymmetry observable in Figs. 2(b)–2(c) and the additional edge states at $\epsilon/J \approx 0$ owe their origin to low-frequency corrections in the effective model (4), which we disregard in the rest of the discussion.

[36] See Supplemental Material at http://link.aps.org/supplemental/10.1103/PhysRevLett.121.075502 for fabrication and characterization of photonic devices, z evolution of optical intensity in a static rhomic lattice ($K = 0$, $\Delta = 0$), more details on AB caging, observation of $8\pi/5$ and 2π

magnetic flux per plaquette, derivation of the effective model with Floquet theory, and mapping to the Creutz ladder.

[37] K. M. Davis, K. Miura, N. Sugimoto, and K. Hirao, Opt. Lett. **21**, 1729 (1996).

[38] D. N. Christodoulides, F. Lederer, and Y. Silberberg, Nature (London) **424**, 817 (2003).

[39] S. Longhi, Laser Photonics Rev. **3**, 243 (2009).

[40] A. Szameit and S. Nolte, J. Phys. B **43**, 163001 (2010).

[41] G. Lenz, I. Talanina, and C. M. de Sterke, Phys. Rev. Lett. **83**, 963 (1999).

[42] N. Chiodo, G. Della Valle, R. Osellame, S. Longhi, G. Cerullo, R. Ramponi, P. Laporta, and U. Morgner, Opt. Lett. **31**, 1651 (2006).

[43] A. Szameit, Y. V. Kartashov, F. Dreisow, M. Heinrich, T. Pertsch, S. Nolte, A. Tünnermann, V. A. Vysloukh, F. Lederer, and L. Torner, Phys. Rev. Lett. **102**, 153901 (2009).

[44] S. Mukherjee, M. Valiente, N. Goldman, A. Spracklen, E. Andersson, P. Öhberg, and R. R. Thomson, Phys. Rev. A **94**, 053853 (2016).

[45] D. R. Hofstadter, Phys. Rev. B **14**, 2239 (1976).

[46] B. A. Bernevig and T. L. Hughes, *Topological Insulators and Topological Superconductors* (Princeton University Press, Princeton, NJ, 2013).

[47] S. J. Bending, K. von Klitzing, and K. Ploog, Phys. Rev. Lett. **65**, 1060 (1990).

[48] F. B. Mancoff, L. J. Zielinski, C. M. Marcus, K. Campman, and A. C. Gossard, Phys. Rev. B **53**, R7599 (1996).

[49] S. Mukherjee, A. Spracklen, D. Choudhury, N. Goldman, P. Öhberg, E. Andersson, and R. R. Thomson, Phys. Rev. Lett. **114**, 245504 (2015).

[50] R. A. Vicencio, C. Cantillano, L. Morales-Inostroza, B. Real, C. Mejía-Cortés, S. Weimann, A. Szameit, and M. I. Molina, Phys. Rev. Lett. **114**, 245503 (2015).

[51] B. Douçot and J. Vidal, Phys. Rev. Lett. **88**, 227005 (2002).

[52] M. Rizzi, V. Cataudella, and R. Fazio, Phys. Rev. B **73**, 144511 (2006).

[53] M. Tovmasyan, S. Peotta, L. Liang, P. Törmä, and S. D. Huber, arXiv:1805.04529.

[54] G. Möller and N. R. Cooper, Phys. Rev. Lett. **108**, 045306 (2012).

[55] D. Leykam, A. Andreanov, and S. Flach, Adv. Phys. X **3**, 1473052 (2018).

[56] See https://doi.org/10.17861/2ed5f3d4-3fed-46be-84f9-ad506c6add6f.

[57] M. Kremer, I. Pedres, E. Meyer, M. Heinrich, O. Zilberberg, and A. Szameit, arXiv:1805.05209.